

# Longitudinal Wind Tunnel Tests of the PROSIB 19-Pax Airplane

Danilo Ciliberti \* , Giuseppe Buonagura and Fabrizio Nicolosi 

Department of Industrial Engineering, University of Naples "Federico II", Via Claudio 21, 80125 Naples, Italy; giu.buonagura@studenti.unina.it (G.B.); fabrnico@unina.it (F.N.)

\* Correspondence: danilo.ciliberti@unina.it

**Abstract:** This research paper delves into the longitudinal wind tunnel tests conducted on the 19-passengers aircraft model of the Italian PROSIB project. The concept is an innovative small air transport airplane with distributed propellers and hybrid-electric powerplant. The primary objective was to assess its stability and control characteristics in power-off conditions. In addition to the usual investigation of the aircraft components, the study introduced a belly-mounted pod, which served as a battery storage unit, and explored two distinct tail configurations: a body-mounted (low) tail and a T-tail (high). The results obtained from these tests generally confirmed the anticipated characteristics of the aircraft design. The experiments provided data on aerodynamic forces and moments, giving useful indications on the effects of a belly-mounted battery storage unit and tail layout on the aircraft stability and control characteristics. This information could be used by aircraft designers to size an airplane of the same class.

**Keywords:** experimental aerodynamics; wind tunnel testing; stability and control; downwash



**Citation:** Ciliberti, D.; Buonagura, G.; Nicolosi, F. Longitudinal Wind Tunnel Tests of the PROSIB 19-Pax Airplane. *Appl. Sci.* **2023**, *13*, 11928. <https://doi.org/10.3390/app132111928>

Academic Editors: Hong Shi, Yujie Guo, Zhaolin Chen and Yan Wang

Received: 19 September 2023

Revised: 20 October 2023

Accepted: 28 October 2023

Published: 31 October 2023



**Copyright:** © 2023 by the authors. Licensee MDPI, Basel, Switzerland. This article is an open access article distributed under the terms and conditions of the Creative Commons Attribution (CC BY) license (<https://creativecommons.org/licenses/by/4.0/>).

## 1. Introduction

The relentless evolution of electrical systems technology has given rise to advancements in hybrid and electric propulsion aircraft [1–4]. These advancements are intrinsically linked with the pursuit of energy efficiency and environmental sustainability in aviation. The Italian national PROSIB project was aimed at developing and investigating innovative configurations for hybrid/electric propulsion systems in both regional fixed-wing aircraft and vertical take-off and landing (VTOL) rotary wing platforms. The project's primary objective was to achieve a substantial reduction of approximately 20% in the energy consumption of air transport by 2035, compared to conventional, non-electric propulsion solutions existing in year 2000. By aligning with the ambitious sustainability objectives set by the International Civil Aviation Organization (ICAO) [5], the PROSIB project endeavored to mitigate the aviation industry's environmental impact.

Several critical components formed the foundation of the PROSIB project's research. As concerns the fixed-wing aircraft, the project ascertained the technological requisites essential for the electrification of aircraft within the regional turboprop class, identifying challenges and constructing a sensible developmental roadmap [6]. Innovations in aircraft configurations spanned from the ATR-42 regional turboprop airplane to the smaller 19-passengers platform, addressing the unique demands of varying operational contexts [7].

This paper deals with the wind tunnel testing of a new 19-passengers airplane model [6], representative of the Small Air Transport (SAT) category identified by the FlightPath 2050 document [8,9]. Although general aviation's emissions impact is relatively minor on a global scale, the SAT segment functions as a crucial bridge, spanning the chasm between experimental aircraft and full-scale commercial aviation. SATs offer a conducive platform for proving and demonstrating diverse technologies, often more effectively than larger passenger aircraft. This is exemplified by the adoption of alternative propulsion systems, initially introduced in light aircraft, which has garnered significant attention in recent years. As such, the SAT segment serves as an ideal avenue for developing comprehensive

aircraft systems, establishing best practices, and charting technological roadmaps for larger aircraft platforms and demonstrators [10].

The use of the wind tunnel for the estimation of aircraft stability and control is as old as the concept itself. Famous manuals and textbooks [11–13] were written by collecting a huge amount of wind tunnel data on aircraft components and configurations. Many of these reports were focusing on a specific aircraft or technique [14–16], while others investigated the effects of component installation on static stability [17–22] or presented advice on test procedures, including propulsive effects [23]. Moreover, there were also experiments focused on the aerodynamic interactions between a scaled model and the walls of the test section, providing procedures to correct wind tunnel data with respect to free flight conditions [24,25]. The wind tunnel is, nowadays, also used to present test cases to the community to validate numerical methods [26,27].

However, most of the literature did not focus on the estimation of the downwash for different wing–tail arrangements, with a few exceptions [22]. Methods for the estimation of the downwash gradient were derived by Silverstein and Katzoff [28] and expanded in USAF DATCOM [12]. Yet, these methods implicitly assume that the tail does not operate within the wing wake, providing a decreasing downwash gradient with the tail distance from the wing, regardless of any wake interaction. In this regard, Spreemann [29], which investigated the wing pitch-up phenomenon, provided a chart indicating the relative wing–tail positions to avoid tail blanketing due to the wing wake. Such a chart was resumed by Raymer [30] in his famous aircraft design book.

The effects of external storage were investigated by several authors, especially on high-speed fighter aircraft [31–33]. The experiments were focused on the best position of an external pylon-mounted pod on either the wing or the fuselage. Apparently, there are few data available on the effects of pods integrated within the fuselage belly. Such arrangements are emerging in new hybrid-electric aircraft concepts, like the Heart Aerospace ES-30 [34] or the Ampaire Eco Caravan [35]. A patent related to a removable cargo pod for light aircraft, invented by Shelton [36], is also available. Among the claims, there is an easy installation and removal of the pod, eliminating unnecessary weight and drag when not needed, but no useful data on the impact of the aircraft performance, stability, and control are presented. The research study conducted by Moonan [37] focused on the analysis of the belly-mounted storage for the NASA's MAPIR (Marshall Airborne Polarimetric Imaging Radiometer) project, installed below a Piper Navajo aircraft. However, the preliminary predictions made with potential flow theory and simplified CFD analyses were invalid because flight tests provided totally different data—thus, the necessity of the experimental investigation of complex aerodynamic systems.

This paper presents the first experimental test campaign on the PROSIB 19-passengers aircraft model to evaluate its power-off longitudinal stability and control characteristics. A rendering of the model is shown in Figure 1. A pod-simulating battery and system storage was conceived to be installed below the fuselage. The pod of the full-scale model would have a useful volume of about 4 m<sup>3</sup>, with the battery occupying about 1.6 m<sup>3</sup> and weighing about 1500 kg, including battery casing, cables, and internal electronics. The remainder of the volume would be shared by the thermal and power management systems, with their own masses and cables. The airplane would have about 55% less block fuel consumption with a battery-specific energy of 270 Wh/kg on a typical 200 nmi mission, with an entry into service forecasted between years 2025 and 2030.

Beyond obtaining the usual aerodynamic coefficients and their derivatives, the project consortium required an investigation of the effects of the integrated battery pod and asked for an experimental comparison between a body-mounted empennage vs. a T-tail configuration. The geometry and sizing of the components were fixed by the preliminary design team and a detailed description of the design process is out of the scope of this work. The experimental data presented in this paper, with the evaluation of the impact of the belly-mounted pod and empennage layout, will be useful to aircraft designers working on the same airplane class.

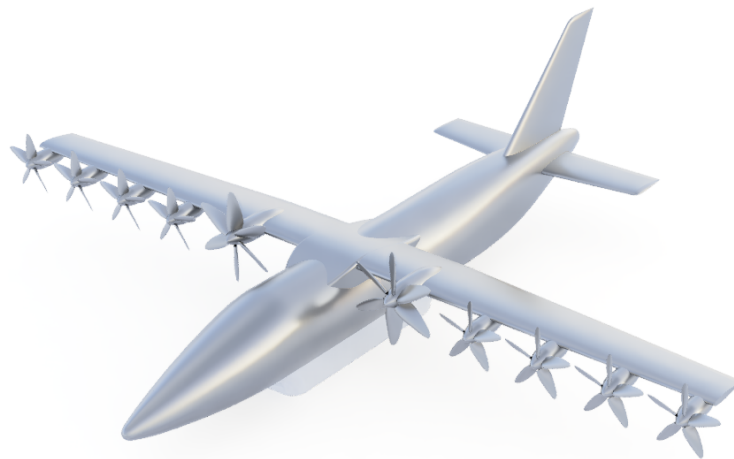


**Figure 1.** Rendering of the PROSIB 19-pax concept.

The remainder of this work is organized as follows. Section 2 presents the experimental setup, along with wind tunnel characteristics, the data acquisition system, the geometry of the test article, and the test matrix. Section 3 discusses the results with a focus on the stability and control derivatives at several flap and elevator deflections. Conclusions are drawn in Section 4.

## 2. Wind Tunnel Setup

### 2.1. Experimental Facility and Equipment

The series of experimental tests have been performed within the primary subsonic wind tunnel facility of the Department of Industrial Engineering. This wind tunnel is a closed-circuit system operating at subsonic speeds and it is equipped with a single return path. Furthermore, the facility is characterized by a closed test section with a tempered rectangular cross-section. The essential components of this wind tunnel are labeled in Figure 2: test section (A–B), the first diffuser (B–C), the second diffuser (D–E), the third diffuser (G–I), the safety screen (C), the first corner (C–D), the second corner (E–F), the third corner (I–L), the fourth corner (L–M), turning vanes within corners, fan ahead the second corner, honeycomb flow straighteners (M), turbulence control screen, stagnation chamber (M), nozzle (M–N). The key features are outlined in Table 1. The measurement equipment includes:

- Longitudinal strain gauge balance;
- Venturi system;
- Inclinator sensor;
- Potentiometer;
- Temperature probe.

**Table 1.** Main characteristics of the wind tunnel.

Characteristic	Value
Test section dimensions	2.0 m × 1.4 m
Maximum available wind speed	50 m/s
Turbulence level	0.10%
Maximum power	150 kW

An internal strain-gauge balance, made in-house with 2024-T3 aluminum alloy, was used to measure lift, drag, and pitching moment. Table 2 offers an overview of the full-scale readings and maximum errors per axis.



- A LabVIEW virtual instrument, developed by the authors to perform data acquisition, data processing, and control the stepper motor.

The virtual instrument was developed with LabVIEW for deployment in the longitudinal wind tunnel test campaign. The application established communication channels with the NI USB-6341 device to acquire the analog signals from the sensors sensible to longitudinal forces and moment, angle of attack, temperature, and dynamic pressure.

To initialize the data acquisition process, a calibration matrix was loaded, along with parameters tailored to the aircraft model and wind tunnel characteristics. All the signals were acquired at a rate of 1000 Hz and averaged on 1000 samples. The strain gauge and Venturi signals were zeroed after the averaging since their voltage at the wind tunnel off was not zero. Thus, their measurements were taken with respect to a reference voltage acquired at the start of the operations. The tilt and temperature sensors had their internal calibration with their own reference voltage and did not need to be zeroed.

After that, the weight components were subtracted from the measured forces and moment at different angles of attack to clear the balance measurements from the effect of the weight and obtain the net aerodynamic forces. Such weight components were preliminarily recorded by changing the pitch of the model at wind tunnel off. This operation is named tare and it was conducted for every investigated configuration.

Standard aerodynamic coefficients have been used to normalize all aerodynamic forces. These coefficients were calculated based on reference parameters: the test section dynamic pressure, the wing mean aerodynamic chord (m.a.c.), and wing planform area as reference parameters. The Reynolds number was determined with respect to the m.a.c. yielding about 430,000. Wind tunnel corrections have been incorporated in the LabVIEW virtual instrument under the procedure outlined in Appendix A.

### 2.3. Aircraft Model Description

The aircraft experimental model was developed by the authors from the design presented in [6] and was made in aluminum alloy, except for the battery pod, which was made with ABS in additive manufacturing. A three-view drawing is provided in Figure 3. The manufacturing and detailed design of the fittings were outsourced. The scale of the model was 1:15, with a wing planform area  $S = 0.25 \text{ m}^2$  and mean aerodynamic chord  $\bar{c} = 0.171 \text{ m}$ . It allowed sufficient internal space to install the strain gauge balance within the fuselage, right below the wing-body fairing. The main connection was between the latter and the balance interface plate. This allowed an easy handling of the components, with the fuselage installed from below. The empennage group could be entirely removed from the fuselage. The airfoils used on the lifting surfaces were the NACA 23018 for the wing root and kink sections, the NACA 23015 for the wingtip section, and the NACA 0012 for the empennage sections.

Two tail configurations were provided: a body-mounted horizontal tail and a T-tail. The latter was designed with the VeDSC method [26] to provide the same directional stability of the former, exploiting the end-plate effect [19]. Under this assumption, the T-tail configuration was sized with about 13% less vertical tail planform area. However, the horizontal tail was scaled down by 30% to be installed on the vertical tail tip. The high horizontal tail had a small backward shift of its aerodynamic center, but it was not sufficient to compensate the loss of planform area and, consequently, of the volumetric coefficient. The two configurations are compared in Figure 4 and their differences are detailed in Table 3. The aerodynamics of the two empennage groups are discussed in the next sections.

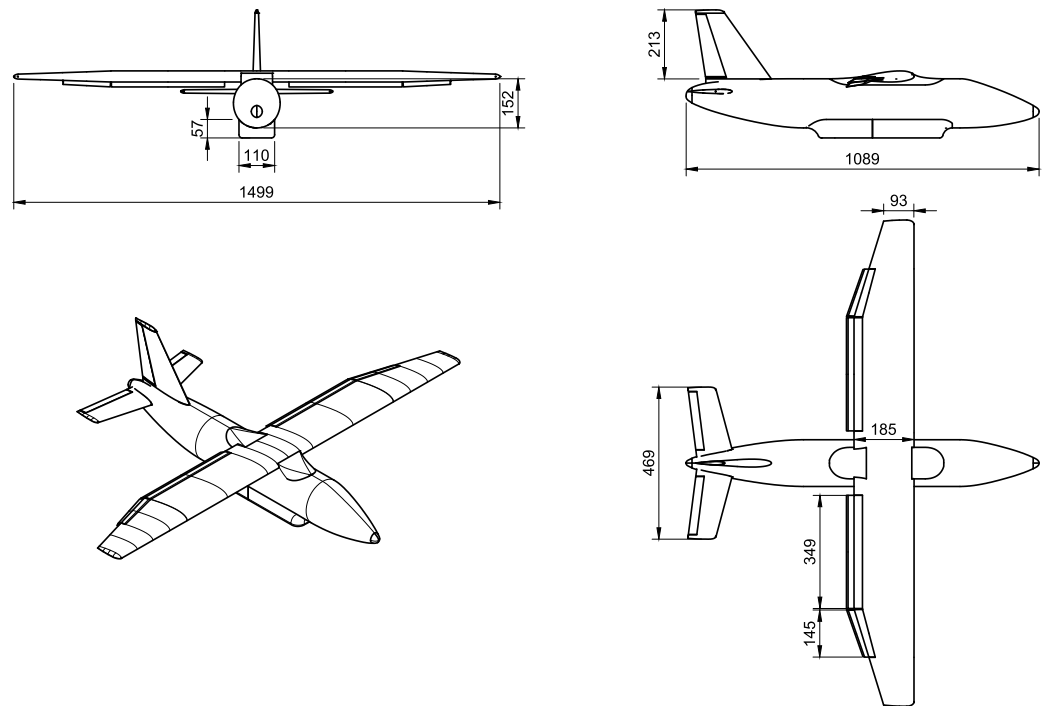


Figure 3. Aircraft model drawings. Units in mm.

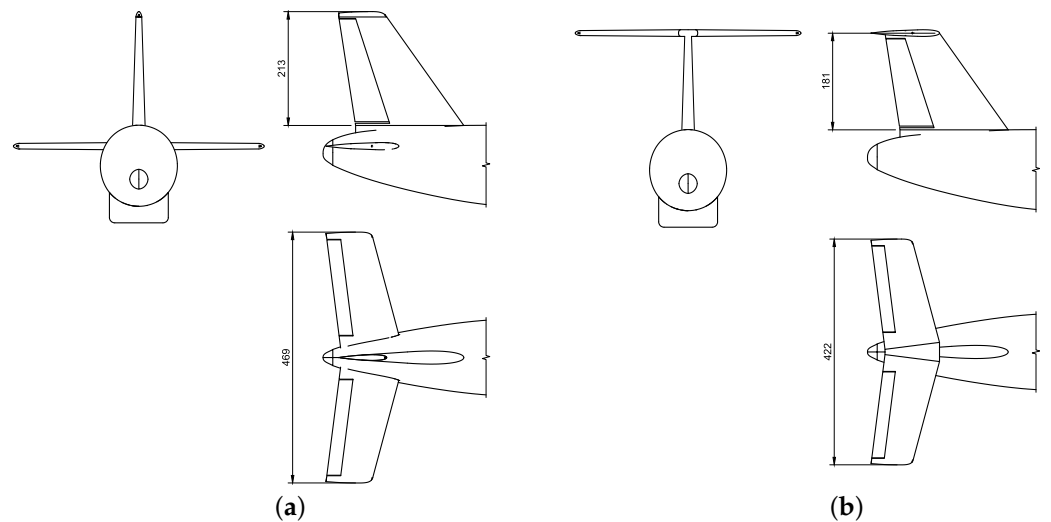


Figure 4. Comparison of two tailplane configurations: (a) body-mounted; (b) T-tail. Units in mm.

Table 3. Comparison of the two horizontal tailplanes data.

Parameter	Body-Mounted	T-Tail
Root chord	123 mm	102 mm
Tip chord	87 mm	77 mm
Span	469 mm	422 mm
Sweep angle	15°	15°
Planform area	49,245 mm <sup>2</sup>	37,769 mm <sup>2</sup>
Aspect ratio	4.47	4.72
Taper ratio	0.71	0.75
Long. distance from ref. point	560 mm	571 mm
Volume tail coefficient	0.645	0.505

2.4. Text Matrix

The nomenclature indicating each aircraft model component is reported in Table 4. Each combination defines the buildup of aircraft components. Underscores separate the configuration layout from the movables state, i.e., flap and elevator. For instance, WBVH\_F15 defines the configuration made up of wing, fuselage, vertical and horizontal tails, with flap deflected by 15°.

**Table 4.** Nomenclature for aircraft components.

Symbol	Description
W	Wing
B	Body (i.e. Fuselage)
Hb	Horizontal tail body-mounted
Ht	Horizontal tail in T-tail configuration
P	Battery pod
–	Separator for movables
F	Flap
E	Elevator

The characterization of the aircraft model stability and control required the planning of a text matrix. The list presented in Table 5 had the aim of simplifying the assembly sequence of several components, accounting for all the possible combinations, including the deflections of the flap and elevator. Preliminary tests were made to install trip strips to force the flow transition near the lifting surface’s leading edges and to evaluate repeatability. These tests are not reported in the test matrix.

**Table 5.** Longitudinal text matrix. Symbols “×” and “/” indicate that a component was installed or not, respectively. All the tests were performed with zero sideslip angle.

	Flap $\delta_f$			Elevator $\delta_e$		
	0°	15°	30°	0°	−10°	−20°
<b>B</b>	/	/	/	/	/	/
<b>BP</b>	/	/	/	/	/	/
<b>BVHb</b>	/	/	/	×		
<b>BVHb</b>	/	/	/		×	
<b>BVHb</b>	/	/	/			×
<b>BVHt</b>	/	/	/	×		
<b>BVHt</b>	/	/	/		×	
<b>BVHt</b>	/	/	/			×
<b>WBVHt</b>	×					×
<b>WBVHt</b>	×					×
<b>WBVHt</b>	×				×	
<b>WBVHt</b>	×			×		
<b>WB</b>	×			/	/	/
<b>WBVHb</b>	×			×		
<b>WBVHb</b>	×				×	
<b>WBVHb</b>	×					×
<b>WBVHb</b>	×					×
<b>WBVHb</b>		×				×
<b>WBVHb</b>		×		×		
<b>WB</b>		×		/	/	/
<b>WBVHt</b>		×		×		

Table 5. Cont.

	Flap $\delta_f$			Elevator $\delta_e$		
	0°	15°	30°	0°	−10°	−20°
WBVHt		×				×
WBVHt			×			×
WBVHt			×	×		
WB			×	/	/	/
WBVHb			×	×		
WBVHb			×			×

### 3. Results and Discussion

The aim of these wind tunnel tests was to evaluate the stability and control characteristics of the innovative commuter aircraft model, including the effects of the belly-mounted battery pod and the empennage configuration (body-mounted vs. T-tail). The results provided a database of aerodynamic derivatives that will be expanded in a future powered test campaign evaluating propulsive effects.

The longitudinal tests were performed by varying the angle of attack of the test article with no sideslip. The aerodynamic forces and moments were evaluated in a body-reference frame with origin at the point of coordinates  $(0.25 \bar{c}, 0.0, -0.20 \bar{c})$  computed from the wing root leading edge. The model was designed such that the strain gauge balance center was right below the estimated position of the wing aerodynamic center. Figure 5 illustrates the relative distances between these three points.

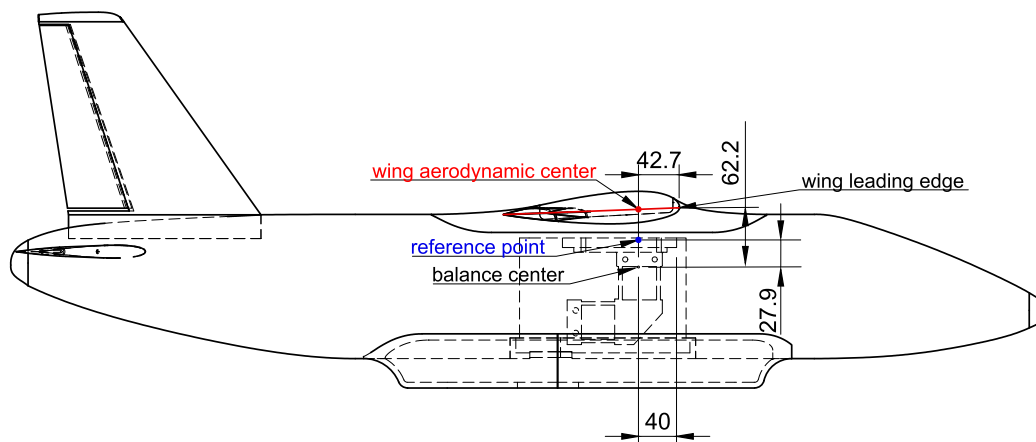


Figure 5. Reference point for the moments. Units in mm.

As the scope of the wind tunnel tests was the evaluation of the characteristics of stability and control, the focus of this section is on the derivatives of the pitching moment  $C_M$  with respect to the angle of attack  $\alpha$  and the elevator deflection  $\delta_e$ . Lift and drag coefficient curves— $C_L$  and  $C_D$ , respectively—have been reported for completeness. However, since the Reynolds number was too low compared to the full-scale flight regime, the stall condition  $C_{L_{max}}$  could not be correctly inferred from the recorded data and the measured drag coefficient was not representative of the real flight conditions. Yet, some indications on the drag contribution of some components can be given with the buildup of aircraft components in the test section.

Repeatability tests have been performed on the wing–body configuration. Repeatability has been evaluated as the standard deviation of the aerodynamic coefficients in the angle of attack range  $-2^\circ$  to  $12^\circ$ . These tests included the effect of installation and configuration change, i.e., they were not three consecutive runs. Table 6 reports the results. Some repeated tests were also performed on other configurations with a similar outcome. The longitudinal



strain gauge balance was behaving as expected, providing a high repeatability on all the variables and a resolution of less than 10 drag counts on the drag coefficient.

**Table 6.** Standard deviation (SD) values of the longitudinal aerodynamic coefficients, evaluated on the wing–body configuration.

	SD ( $\alpha$ , deg)	SD ( $C_L$ )	SD ( $C_D$ )	SD ( $C_M$ )
avg.	0.034	0.0051	0.0007	0.0006
min	0.015	0.0029	0.0002	0.0002
max	0.047	0.0062	0.0010	0.0010

### 3.1. Wing–Body Contribution

The wing–body configuration was evaluated with the three available flap deflections, as shown in Figure 6. Results are reported in Figure 7. As the flap was of a Fowler type, the increase in the slope of the lift curve in addition to its upward shift is apparent. The deflection of the flaps increased the lift coefficient at the zero angle of attack  $C_{L_0}$  by 0.35 with  $\delta_f = 15^\circ$  and by a further 0.40 with  $\delta_f = 30^\circ$ . The wing lift curve slope  $C_{L_\alpha}$  increased from  $0.073 \text{ deg}^{-1}$  in clean configuration to  $0.092 \text{ deg}^{-1}$  in a flapped configuration. The stall was anticipated at a lower angle of attack, whereas drag and pitching moment magnitude increased.

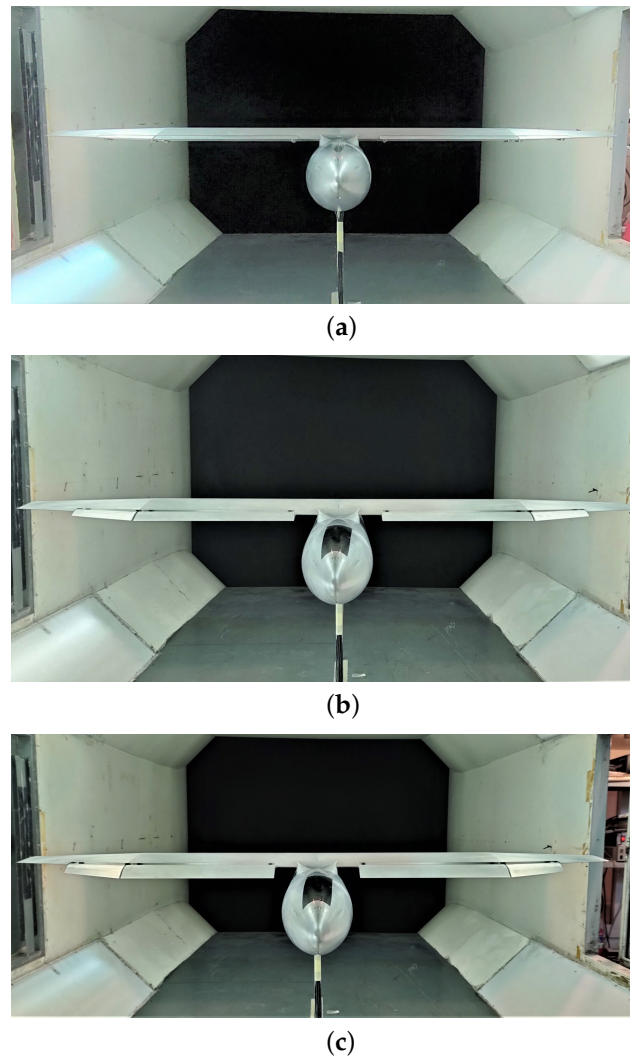
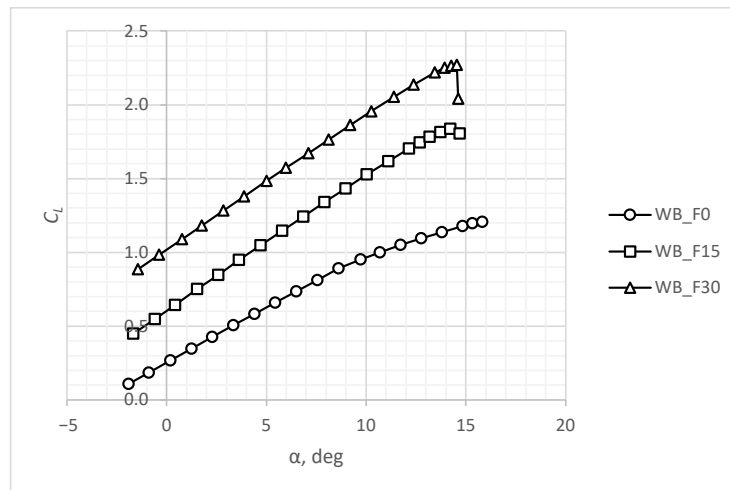
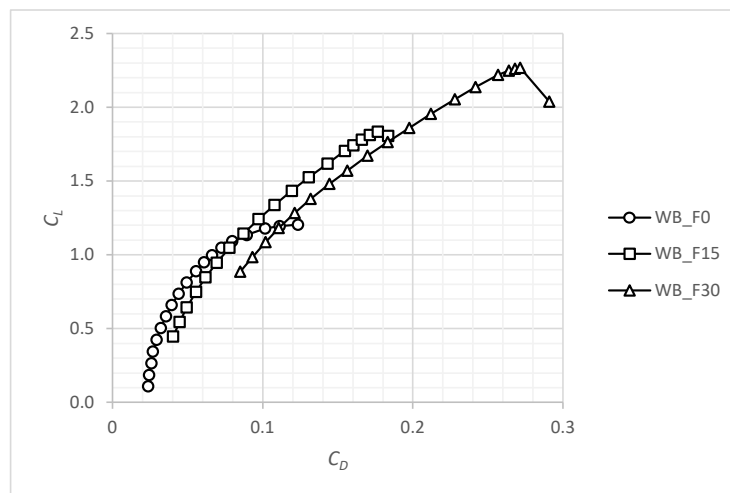


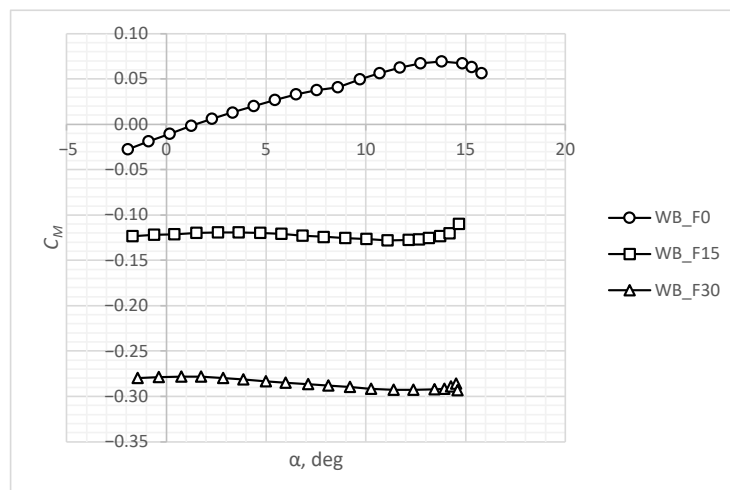
**Figure 6.** Wing body configurations: (a) flap deflected at  $0^\circ$ ; (b) flap deflected at  $15^\circ$ ; (c) flap deflected at  $30^\circ$ .



(a)



(b)



(c)

**Figure 7.** Aerodynamic curves for the wing–body configuration: (a) lift curves; (b) drag polars; (c) pitching moment curves.

The slope of the pitching moment coefficient with respect to the angle of attack is related to the measure of aircraft longitudinal stability. The derivative  $C_{M_\alpha}$  was equal to  $0.007 \text{ deg}^{-1}$  for the clean configuration, whereas it was reduced to about zero with the

flaps deflected. The values achieved by the wing–body combination indicated its unstable contribution to aircraft longitudinal stability with respect to the chosen reference point.

From the acquired data, it was possible to estimate the non-dimensional location of the wing–body aerodynamic center  $\bar{x}_{a.c.WB}$  for the clean configuration, whose shift from the moment reference point was evaluated as the opposite of the ratio of the pitching moment curve slope and the lift curve slope:

$$\bar{x}_{a.c.WB} = \bar{x}_{ref} - \frac{C_{M_{\alpha, WB}}}{C_{L_{\alpha, WB}}} = 0.25 - \frac{0.007}{0.073} = 0.153 \quad (1)$$

indicating that it was located at a distance of 15.3% m.a.c. length ahead of the chosen reference point.

Although an estimation for the flapped configurations could be made with Equation (1), since their pitching moment curves were quite flat, it was apparent that the flap deflection shifted the aerodynamic center back to the 25% of the m.a.c. As previously stated, the deflection of the flap also caused a shift of the pitching moment at the zero angle of attack  $C_{M_0}$  by  $-0.11$  for  $\delta_f = 15^\circ$  and by a further  $-0.15$  for  $\delta_f = 30^\circ$ . These additional values of the pitching moment coefficient have to be balanced by the horizontal tailplane in the full aircraft configuration to keep the longitudinal equilibrium at the desired lift coefficient.

### 3.2. Effects of the Empennage Configuration

The scope of the horizontal tailplane is to introduce longitudinal stability and provide longitudinal control in a conventional aircraft layout. In this section, a comparison between the two tailplane configurations shown in Figure 8 is made.



**Figure 8.** Photographs of the two tailplanes: (a) body-mounted configuration; (b) T-tail configuration.

The configurations analyzed were the WBVH—the complete aircraft without the battery pod—with three flap deflections. These are illustrated in Figure 9.

The results of the wind tunnel runs are shown in Figure 10. These were untrimmed conditions with the elevator deflection  $\delta_e = 0^\circ$ . The lift curve slope  $C_{L_{\alpha}}$  was about 10% higher than that of the wing–body configuration due to the presence of the horizontal tail. There was no appreciable difference between the lift provided by the two tail configurations.

With respect to the wing–body configuration, the drag coefficient has been increased due to the additional contribution of the empennage. The body-mounted tail was slightly more efficient than the T-tail with the flap deflected for landing ( $\delta_f = 30^\circ$ ). However, the aerodynamic efficiency—the lift-to-drag ratio—is not important in landing conditions, where the aircraft has to slow down.

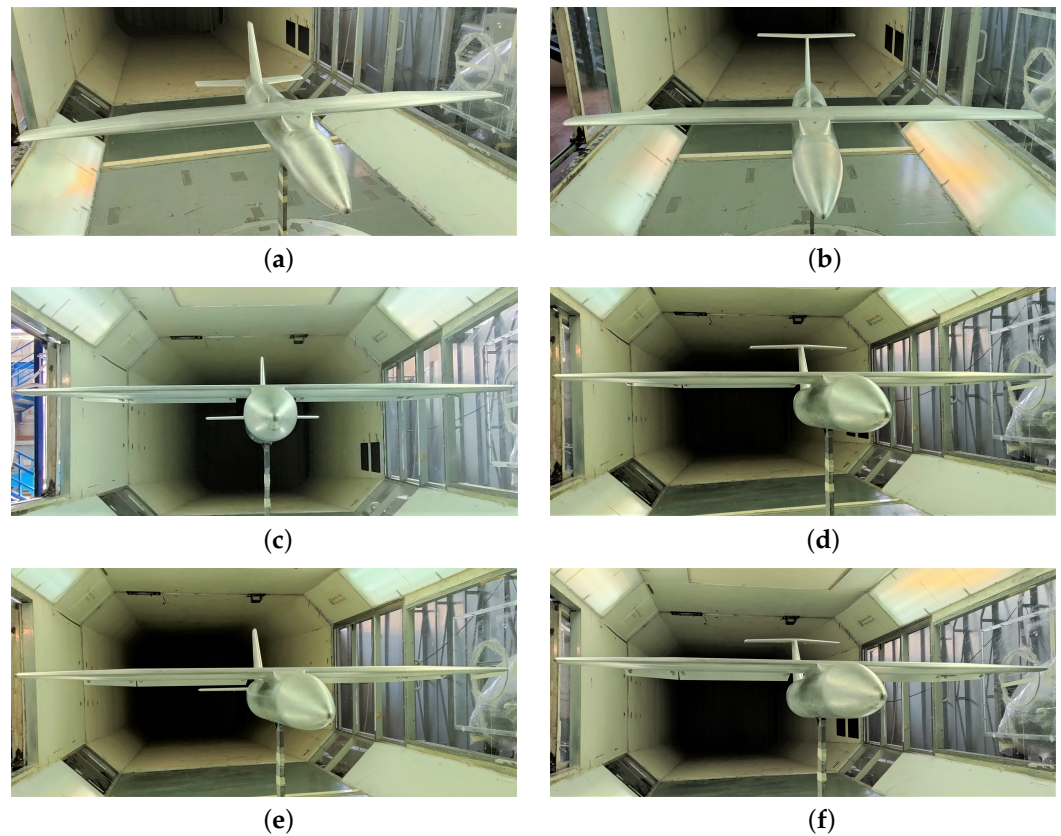


**Figure 9.** Complete aircraft configurations with different tailplanes and three flap deflections: (a) WB-VHb\_F0; (b) WBVHt\_F0; (c) WBVHb\_F15; (d) WBVHt\_F15; (e) WBVHb\_F30; (f) WBVHt\_F30.

The pitching moment curves presented larger differences, with the body-mounted tail slightly more stable than the T-tail with increasing flap deflection. The values for  $C_{M_0}$ ,  $C_{M_\alpha}$ , and  $C_{M_{\delta_f}}$  for the two empennage with different flapped deflections are reported in Table 7. These values have been obtained with a linear regression on the angle of attack range  $-2^\circ$  to  $10^\circ$ . The reported quantities have been defined as follows:

$C_{M_0}$  is the intercept of the regression line;

$C_{M_\alpha}$  is the slope of the regression line;

$C_{M_{\delta_f}}$  is the shift between the  $C_{M_0}$  at  $\delta_f \neq 0^\circ$  and the  $C_{M_0}$  at  $\delta_f = 0^\circ$  scaled by the value of deflection  $\delta_f$ .

More generally, a control power derivative was evaluated as the incremental ratio of  $C_{M_0}$  with the deflection angle  $\delta$ , with zero as the initial point. The expression is as follows:

$$C_{M_\delta} = \frac{C_{M_0}(\delta) - C_{M_0}(\delta = 0^\circ)}{\delta} \tag{2}$$

**Table 7.** Values of pitching moment characteristics for the WBVH configuration at different flap deflections. Elevator deflection  $\delta_e = 0^\circ$ . Derivatives in  $\text{deg}^{-1}$ .

$\delta_f$	Body-Mounted Tail (Hb)			T-Tail (Ht)		
	$0^\circ$	$15^\circ$	$30^\circ$	$0^\circ$	$15^\circ$	$30^\circ$
$C_{M_0}$	0.0441	-0.0460	-0.1592	0.0383	-0.0231	-0.1385
$C_{M_\alpha}$	-0.0181	-0.0206	-0.0241	-0.0157	-0.0205	-0.0218
$C_{M_{\delta_f}}$	n.a.	-0.0060	-0.0068	n.a.	-0.0041	-0.0059

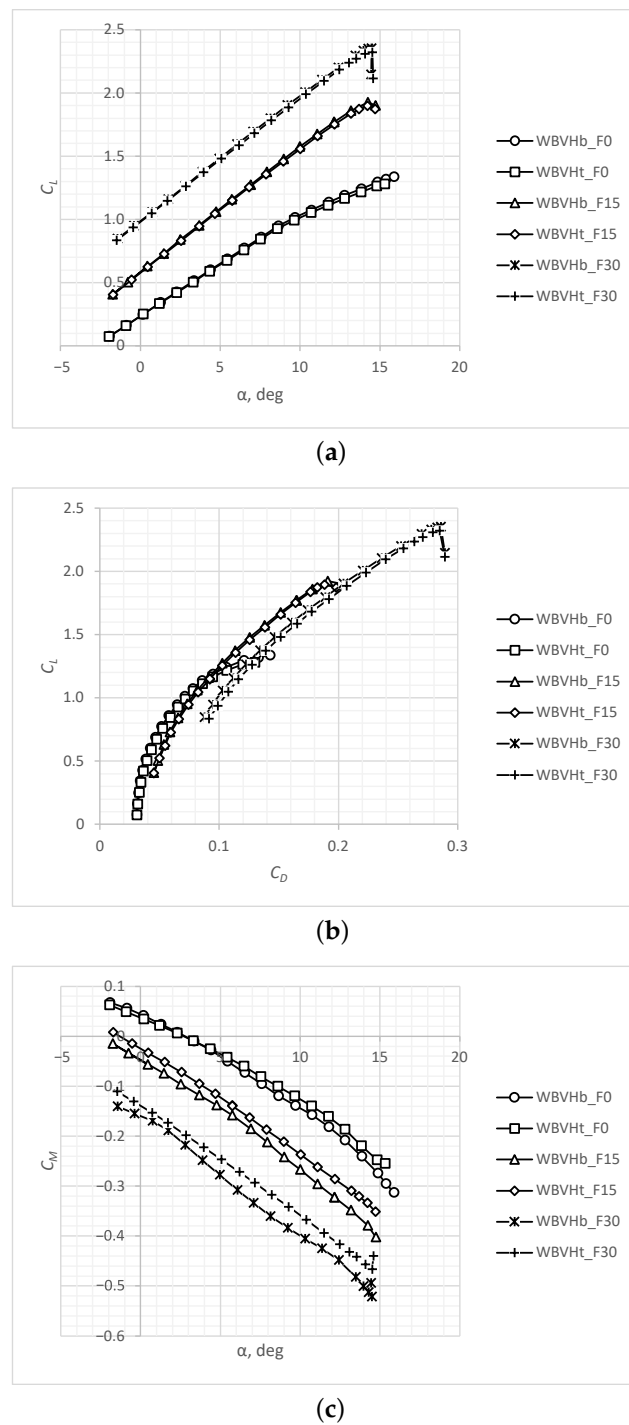


**Figure 10.** The effects of the flaps on the aerodynamic curves of the complete aircraft without the battery pod: (a) lift curves; (b) drag polars; (c) pitching moment curves.

The configurations of the complete aircraft model with clean wing ( $\delta_f = 0^\circ$ ) and several elevator angles  $\delta_e$  were also analyzed to evaluate the horizontal tail control power. Examples of elevator deflections are illustrated in Figure 11 for the two horizontal tail configurations. The main effect of a negative elevator deflection was to shift upward the pitching moment curve. This allowed the aircraft to achieve the longitudinal equilibrium at a higher angle of attack. A secondary effect was a minor shift in the lift curve in the opposite direction and a small increase in the aerodynamic drag, as shown in Figure 12. It is here remarked that the curves labeled WBVHb\_F0 in Figure 10 and WBVHb\_E0 in

Figure 12 represent the same run, as well as WBVHt\_F0 in Figure 10 and WBVHt\_E0 in Figure 12.

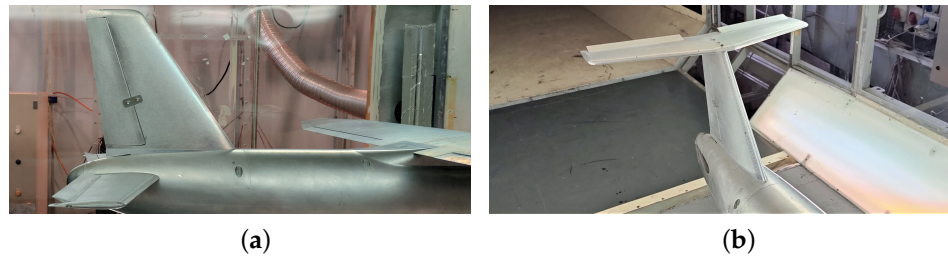
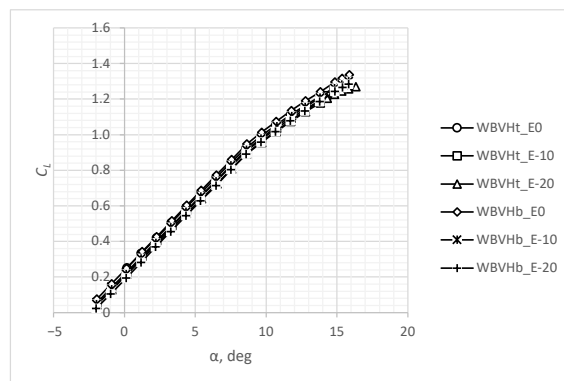
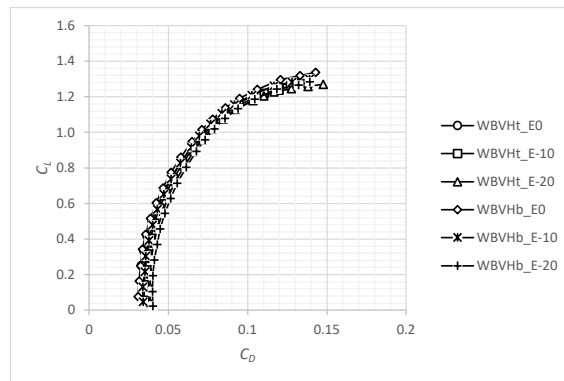


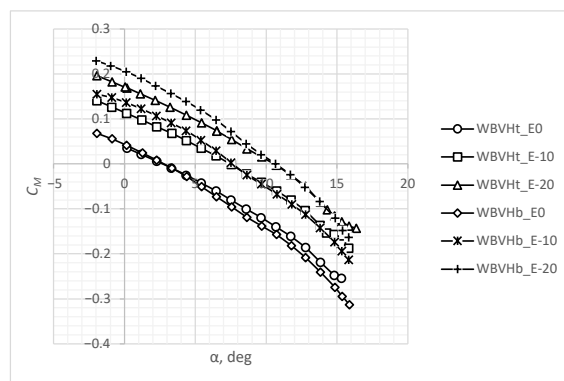
**Figure 11.** Detail of the elevator deflection  $\delta_e = -20^\circ$  for the two tail configurations: (a) body-mounted tail; (b) T-tail.



(a)



(b)



(c)

**Figure 12.** The effects of the elevators on the aerodynamic curves of the complete aircraft without the battery pod: (a) lift curves; (b) drag polars; (c) pitching moment curves.

It is apparent that the shift in  $C_{M_0}$  was larger for the body-mounted configuration, indicating a more powerful longitudinal control. The values for  $C_{M_0}$ ,  $C_{M_\alpha}$ ,  $C_{M_{\delta_e}}$ , and zero-lift drag coefficient  $C_{D_0}$  for the different elevator deflections are reported in Table 8. The last derivative is the elevator control power. Generally speaking, a control power derivative is supposed to be constant for small deflections. The decrease of  $C_{M_{\delta_e}}$  with  $\delta_e$  indicated a loss of elevator effectiveness due to non-linear effects attributed to flow separation on the control surface.

A comparison has been made among the values of the zero-lift drag coefficient  $C_{D_0}$ . It has been evaluated as the intercept of the regression line  $C_D$  vs.  $C_L^2$ , where the squared lift coefficient has been used to linearize the drag polar data. The last row of Table 8 is a measure of the trim drag.

**Table 8.** Values of pitching moment characteristics and zero-lift drag coefficient for the WBVH configuration at different elevator deflections. Flap deflection  $\delta_f = 0^\circ$ . Derivatives in  $\text{deg}^{-1}$ .

$\delta_e$	Body-Mounted Tail (Hb)			T-Tail (Ht)		
	$0^\circ$	$-10^\circ$	$-20^\circ$	$0^\circ$	$-10^\circ$	$-20^\circ$
$C_{M_0}$	0.0441	0.1385	0.2073	0.0383	0.1155	0.1765
$C_{M_\alpha}$	-0.0181	-0.0176	-0.0179	-0.0157	-0.0155	-0.0162
$C_{M_{\delta_e}}$	n.a.	-0.0094	-0.0082	n.a.	-0.0077	-0.0069
$C_{D_0}$	0.029	0.032	0.038	0.030	0.033	0.036

The stability derivatives were evaluated at the zero angle of attack, but it is interesting to note that in Figure 12c, the slopes of the curves of the two different tails around the trim points—where  $C_M = 0$ —are practically the same. Since the aircraft will spend most of the time in equilibrium conditions, it could be argued that the two horizontal tails will provide almost the same longitudinal stability most of the time. However, an aircraft must be stable and controllable throughout the flight envelope; thus, all the considerations made on the different contributions of the two empennage still hold.

The downwash gradient  $d\varepsilon/d\alpha$  is a measure of the influence of the wing wake on the horizontal tailplane. Such a measure was obtained with an approach similar to that presented in [22], as the ratio of the  $C_{M_\alpha}$  of the tail in combinations with and without the wing. The effect of the tail within a given combination of components was obtained as the difference of  $C_{M_\alpha}$  of those combinations with and without the tail. The expression is:

$$\left(1 - \frac{d\varepsilon}{d\alpha}\right) \approx \frac{\overbrace{C_{M_{\alpha, \text{WBH}}} - C_{M_{\alpha, \text{WB}}}}^{(C_{M_{\alpha, \text{H}}})_{\text{WBH}}}}{\underbrace{C_{M_{\alpha, \text{BH}}} - C_{M_{\alpha, \text{B}}}}_{(C_{M_{\alpha, \text{H}}})_{\text{BH}}}} \tag{3}$$

where the variation in dynamic pressure between the wing-on and the wing-off configurations has been assumed to be the same.

A synopsis of these data has been reported in Table 9, where the charts of the WBH runs have been omitted for the sake of brevity. Again, the body-mounted horizontal tail proved to be more effective than the T-tail, having a lower downwash value. This was attributed to the wing–tail relative position in the two different configurations. As a matter of fact, the wake of the high wing moved closer to the T-tail with an increasing angle of attack. Conversely, the wing wake moved away from the body-mounted tail with an increasing angle of attack. The T-tail also had a 28% less volume coefficient, as previously reported in Table 3. Thus, the comparison was not between the same horizontal tail at different locations but between two similar tailplanes. Both tail configurations with wing flap deflection achieved larger values of the downwash gradient and, except for a small difference with  $\delta_f = 15^\circ$ , the estimations confirmed the previous trend. The T-tail in this

specific high wing configuration provided less longitudinal stability than the larger body-mounted tail. However, even if the high horizontal tail had the same planform area of the low horizontal tail, the values of the downwash gradient would not have significantly changed from those previously estimated. The influence of the wing wake on the tail does not depend on the tail size—for tailplanes whose aspect ratio is quite a bit smaller than that of the wing—but only on their relative positions and on wing planform shape.

**Table 9.** Evaluation of the downwash gradient for the two empennage configurations. Aerodynamic derivatives in  $\text{deg}^{-1}$ . The downwash gradient is a dimensionless quantity.

	$C_{M_{\alpha,B}}$	$C_{M_{\alpha,WB}}$	$C_{M_{\alpha,BH}}$	$C_{M_{\alpha,WBH}}$	$\left(1 - \frac{d\epsilon}{d\alpha}\right)$	$\frac{d\epsilon}{d\alpha}$
Hb, $\delta_f = 0^\circ$	0.0056	0.0059	−0.0267	−0.0201	0.805	0.195
Ht, $\delta_f = 0^\circ$	0.0056	0.0059	−0.0249	−0.0167	0.741	0.259
Hb, $\delta_f = 15^\circ$	0.0056	−0.0003	−0.0267	−0.0211	0.644	0.356
Ht, $\delta_f = 15^\circ$	0.0056	−0.0003	−0.0249	−0.0208	0.672	0.328
Hb, $\delta_f = 30^\circ$	0.0056	−0.0012	−0.0267	−0.0241	0.709	0.291
Ht, $\delta_f = 30^\circ$	0.0056	−0.0012	−0.0249	−0.0218	0.675	0.325

### 3.3. Effects of the Battery Pod

The battery pod was installed on the belly of the aircraft model, as shown in Figure 13. With its length and cross-section, it affected the aerodynamic drag and the longitudinal stability. The pod was investigated on the body configuration only. Since there was no appreciable lift generated, only the drag polars and the pitching moment curves are presented in Figure 14. The increment in zero-lift drag coefficient  $C_{D_0}$  was about 0.0050. The fuselage alone provided 76 drag counts. The significant addition of 50 drag counts due to the pod has been attributed to:

- Surface roughness of the pod material (ABS plastics), providing a larger skin friction drag than polished aluminum;
- Aerodynamic interference of the support strut crossing the pod;
- Pressure drag due to the pod blunt shape.

Both body and body-pod combinations exhibited a linear variation of drag coefficient with lift coefficient. However, the presence of the pod also changed the slope of the drag curve. The slopes  $dC_D/dC_L$  were 0.2297 and 0.5362, respectively, for the body and the body-pod configurations.

The pod did not alter the fuselage planform view, but only the cabin cross-section and side view. The pitching moment curves were parallel on most of the data points, as expected. Nevertheless, an 18% reduction in  $C_{M_\alpha}$  for the body-pod combination has been measured in the angle of attack range  $-2^\circ$  to  $5^\circ$ , with a 0.002 decrement in  $C_{M_0}$  magnitude. The reduction in the body unstable contribution to longitudinal stability was attributed to the blunt shape of the pod, which may have generated a pitch-down contribution at low angles of attack.

Since the pod and the wing were installed in opposite locations, no additional aerodynamic interference was expected with other component combinations.

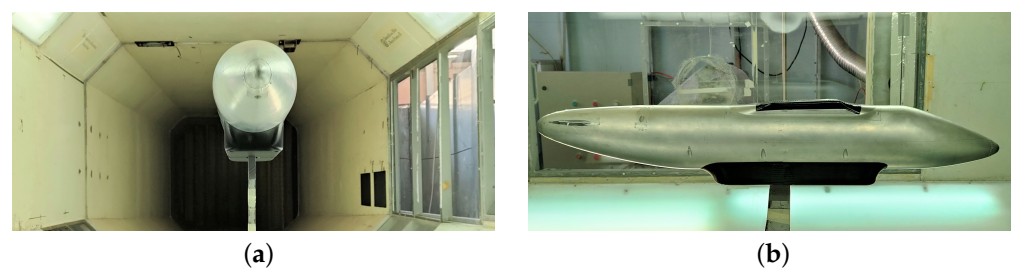
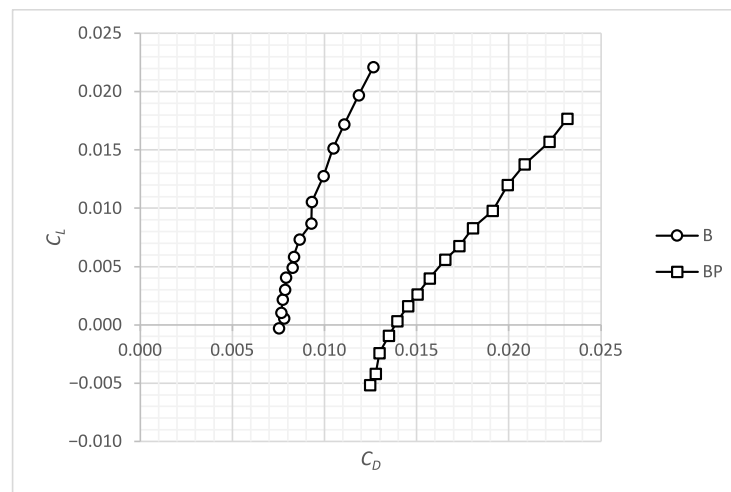
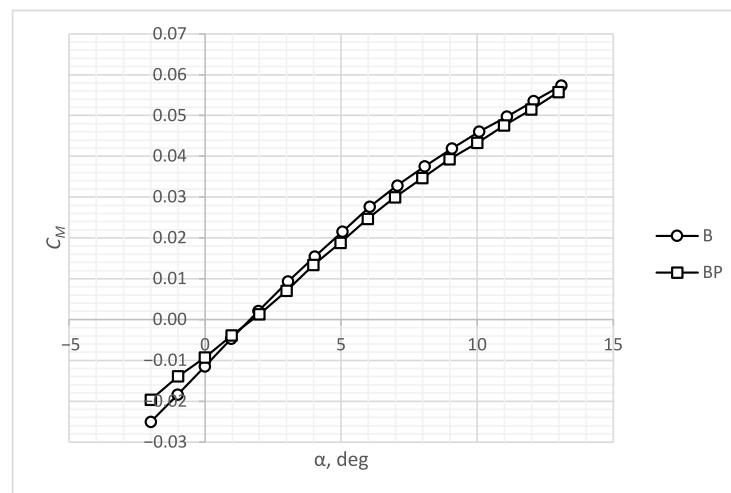


**Figure 13.** Body-pod configuration: (a) front view; (b) side view.





(a)



(b)

**Figure 14.** The effects of the battery pod: (a) drag polars; (b) pitching moment curves.

#### 4. Conclusions

The paper has presented the longitudinal wind tunnel investigations of the PROSIB 19-passengers airplane. The experimental tests at low speed were necessary to evaluate the stability and control characteristics of the aircraft. Although the attained low Reynolds number did not allow us to infer realistic values for the drag coefficient and the maximum lift coefficient, the wind tunnel data were useful to evaluate the stability and control derivatives for the complete aircraft configuration as well as combinations of its components. All the configurations with the wing involved the analysis of the effect of the flap deflection. All the configurations with the tail were made at different elevator deflections.

The investigation on the wing–body configuration provided data on the aerodynamics of the high-lift system—the increment in lift, drag, and pitching moment coefficients. These measures allowed an estimation of the aerodynamic center position, which on the clean wing was shifted forward by about the 15% of the m.a.c. length from the reference point. Conversely, the deflection of the flaps provided a shift in the wing–body aerodynamic center back to the reference point location.

Two empennage configurations were evaluated: a body-mounted horizontal tail and a T-tail configuration. The latter provided 14% less longitudinal stability and 18% less longitudinal control power than the former. This was attributed to the smaller planform area and to the shorter vertical distance of the horizontal tail to the high wing, which caused the wake of the latter to be closer to the former than in the case of the body-mounted tail.

However, the main objective of the T-tail was to provide the same directional stability of the larger vertical tail of the body-mounted configuration. The validation of this statement is the argument of a future paper.

The downwash effect, which characterizes the longitudinal stability and affect tail design was also estimated. The values of the downwash gradient of the T-tail were larger than those of the body-mounted tail with all flap deflections, up to 30% for the clean wing configuration. This confirmed the statements of the previous paragraph and the importance of experiments over preliminary methods of analyses. Although the comparison between the two tail configurations was not completely fair due to the different values of the volumetric ratio, the downwash gradient should be unaffected by the tail size. Also, the reduced restoring moment provided by the T-tail was not critical for aircraft longitudinal stability, which was investigated within the range of angles of attack of interest. However, it would be better to avoid a T-tail configuration for an airplane layout similar to the model investigated in this paper.

The effects of the belly container were also investigated. The installation of the pod provided a significant increase of the zero-lift drag by 50 drag counts and doubled the drag-due-to-lift factor. This was attributed to the blunt shape of the pod, which also provided an 18% reduction of the body group unstable contribution to longitudinal stability, as well as interference effects with the model support strut.

Finally, although information on lift and pitching moment were given throughout Section 3, a synopsis table on the longitudinal characteristics is presented in Table 10. The first and last columns represent the zero-lift angle of attack  $\alpha_{0L}$  and the non-dimensional position of the aerodynamic center  $\bar{x}_{a.c.}$ , respectively. Both make no sense for combinations without the wing. The aerodynamic center of the WBVH configurations represents the neutral point of the aircraft, which is the rear limit of the center of gravity position to obtain a statically stable airplane.

**Table 10.** Synopsis of the lift and pitching moment characteristics, including aerodynamic center coordinates.

Configuration	$\alpha_{0L}$ (deg)	$C_{L_0}$	$C_{L_\alpha}$ (deg <sup>-1</sup> )	$C_{M_0}$	$C_{M_\alpha}$ (deg <sup>-1</sup> )	$\bar{x}_{a.c.}$
B	n.a.	0.00	0.001	-0.011	0.007	n.a.
BP	n.a.	0.00	0.001	-0.009	0.006	n.a.
BVHb	n.a.	-0.01	0.011	0.005	-0.025	n.a.
BVHt	n.a.	-0.01	0.010	0.012	-0.024	n.a.
WB_F0	-3.4	0.25	0.073	-0.011	0.007	0.159
WB_F15	-6.5	0.61	0.093	-0.121	0.000	0.252
WB_F30	-11.1	1.02	0.092	-0.278	-0.001	0.262
WBVHb_F0	-2.9	0.24	0.082	0.044	-0.018	0.472
WBVHb_F15	-5.8	0.58	0.100	-0.046	-0.021	0.457
WBVHb_F30	-9.9	0.99	0.099	-0.159	-0.024	0.492
WBVHt_F0	-2.9	0.24	0.080	0.038	-0.016	0.446
WBVHt_F15	-5.8	0.58	0.099	-0.023	-0.020	0.457
WBVHt_F30	-10.0	0.98	0.098	-0.139	-0.022	0.473

Future works will provide a discussion on the lateral-directional characteristics, including the combined runs, e.g., the effects of the flap in sideslip. Also, a new test campaign involving distributed propellers has been planned to evaluate the effects of such innovative powertrains on aircraft stability and control.

**Author Contributions:** Conceptualization, D.C. and G.B.; methodology, D.C. and F.N.; software, D.C. and G.B.; validation, D.C., G.B. and F.N.; formal analysis, D.C., G.B. and F.N.; investigation, G.B. and F.N.; resources, F.N.; data curation, D.C. and G.B.; writing—original draft preparation, D.C. and G.B.; writing—review and editing, D.C., G.B. and F.N.; visualization, D.C., G.B. and F.N.; supervision, F.N.; project administration, F.N.; funding acquisition, F.N. All authors have read and agreed to the published version of the manuscript.

**Funding:** This research was funded by the Italian PROSIB (Propulsione e Sistemi Ibridi per velivoli ad ala fissa e rotante—Hybrid Propulsion and Systems for fixed and rotary wing aircraft) project PNR 2015-2020 lead by Leonardo S.p.A.

**Institutional Review Board Statement:** Not applicable.

**Informed Consent Statement:** Not applicable.

**Data Availability Statement:** The authors confirm that the data supporting the findings of this study are available within the article.

**Acknowledgments:** The authors would like to thank their colleagues Vincenzo Cusati and Valerio Marciello for a fruitful discussion on the preliminary design process of the aircraft concept investigated in this paper.

**Conflicts of Interest:** The authors declare no conflict of interest. The funders had no role in the design of the study; in the collection, analyses, or interpretation of data; in the writing of the manuscript; or in the decision to publish the results.

### Abbreviations

The following abbreviations are used in this manuscript:

B	Body or fuselage
E	Elevator
F	Flap
Hb	Horizontal tail installed in the fuselage (body-mounted)
Ht	Horizontal tail installed on the tip of the vertical tail (T-tail)
ICAO	International Civil Aviation Organization
m.a.c.	Mean aerodynamic chord
P	Pod
PC	Personal computer
PROSIB	Propulsione e Sistemi Ibridi per velivoli ad ala fissa e rotante
SAT	Small air transport
V	Vertical tail
VeDSC	Vertical tail design, stability, and control
VTOL	Vertical take-off and landing
W	Wing
$\mathcal{R}$	Aspect ratio
$C_D$	Drag coefficient
$C_L$	Lift coefficient
$C_M$	Pitching moment coefficient
$\bar{c}$	Mean aerodynamic chord
$S$	Wing planform area
$\bar{x}_{a.c.}$	Aerodynamic center coordinate
$\bar{x}_{ref}$	Reference point coordinate
$\alpha$	Angle of attack
$\alpha_{0L}$	Zero-lift angle of attack
$\delta_e$	Elevator deflection angle
$\delta_f$	Flap deflection angle
$\varepsilon$	Downwash angle
$C(\cdot)_0$	Aerodynamic coefficient evaluated at $\alpha = 0$ , except $C_{D_0}$ that is evaluated at $C_L = 0$
$C(\cdot)_\alpha$	Aerodynamic derivative with respect to $\alpha$
$C(\cdot)_{\delta_e}$	Aerodynamic derivative with respect to $\delta_e$
$C(\cdot)_{\delta_f}$	Aerodynamic derivative with respect to $\delta_f$

### Appendix A. Wind Tunnel Corrections

The challenges inherent in conducting wind tunnel testing, as well as the necessity for corrections to account disparities between wind tunnel conditions and real-world scenarios, constitute the central focus of the discussion. Various effects are defined and elucidated:

- Horizontal buoyancy: the presence of solid walls in a wind tunnel creates static pressure variations along the test section, leading to an increase in drag known as the buoyancy effect.
- Solid blockage: it refers to the reduction in stream cross-sectional area due to the model presence in the wind tunnel, leading to variations in oncoming flow speed or dynamic pressure. It is a noteworthy factor affecting measurements.
- Wake blockage: bodies in motion within a fluid generate wakes. In a wind tunnel, the lowered pressure that occurs when the boundary layer, which later becomes wake, grows on the model, resulting in an overestimation of drag due to the increased pressure gradient.
- Streamline curvature: the curvature of flow streamlines around a model in a wind tunnel differs from those in an infinite stream. This alteration affects lift, pitching moment, hinge moments, and angle of attack, causing them to increase when measured in a closed section tunnel.
- Normal downwash change: due to finite distances to boundaries, the induced flow in the lift direction changes, affecting lift and drag measurements. A closed jet environment provides a smaller downwash with respect to an unbounded stream.
- Spanwise downwash distortion: the local angle of attack distribution along the span of a lifting surface is altered in a closed test section and the angle of attack at the wingtips is increased. This can impact the onset of the tip stall starting at a lower geometric angle of attack.
- Tail downwash change: the alteration of downwash behind the wing in a closed jet leads to changes in the wing wake location, which is higher than in free air. As a result, the static stability of the model increases.

### Appendix A.1. Mathematical Models

The mathematical models of the applied correction are here described. The premise is that, compared to the literature, the corrections implemented so far are affected by further approximations. For instance, Barlow et al. [25] apply the corrections referring to the wing lift coefficient  $C_{LW}$ , while in our data acquisition software, they are based on total lift coefficient  $C_L$ . To enhance readability, comparisons with the literature have been added as footnotes. The wind tunnel corrections are applied in this sequence:

1. Solid blockage  $\epsilon_{sb}$  and wake blockage  $\epsilon_{wb}$ ;
2. Dynamic pressure ratio  $q_c/q$ ;
3. Angle of attack variation  $\Delta\alpha$ ;
4. Lift coefficient variation  $\Delta C_L$ ;
5. Drag coefficient variation  $\Delta C_D$ ;
6. Pitching moment variation  $\Delta C_M$ .

Historically [24,25], wind tunnel corrections were focused on longitudinal quantities. Lateral-directional corrections account only for blockage effects and dynamic pressure. All the corrections here presented are valid for a closed return, closed test section wind tunnel.

#### Appendix A.1.1. Solid Blockage

It is the most important effect. It depends on the size of the model compared to the volume of the test section. This effect increases the effective velocity of the air on the model and consequently the dynamic pressure. It is the sum of the blockages of the individual components:

$$\epsilon_{sb,i} = \frac{K_1 \tau_1 (\text{wing volume})_i}{C^{3/2}} \quad \text{or} \quad \frac{K_3 \tau_1 (\text{body volume})_i}{C^{3/2}} \tag{A1}$$

$$\epsilon_{sb} = \sum_i \epsilon_{sb,i} \tag{A2}$$

where  $K_1$  and  $K_3$  are the body shape factors, defined through charts provided in (Ref. [25], §10.2);  $\tau_1$  is a factor depending on the tunnel test-section shape and the model span-to-tunnel-width ratio, evaluated with another chart of (Ref. [25], §10.2);  $C$  represents the tunnel test cross-sectional area.

#### Appendix A.1.2. Wake Blockage

It is typically a negligible factor compared to the solid blockage. This effect depends on the wake of the test model, leading to an increase in the effective air velocity on the model and an increase in the aerodynamic drag in a wind tunnel with a closed test section. Each individual component has a wake blockage described by Equation (A3), whereas the total wake blockage is expressed by Equation (A4):

$$\epsilon_{wb,i} = \frac{S}{4C} C_{D0,i} \tag{A3}$$

$$\epsilon_{wb} = \sum_i \epsilon_{wb,i} \tag{A4}$$

parameter  $S$  is the planform area of the wing and  $C$  is, again, the tunnel test cross-sectional area. To estimate  $\epsilon_{wb}$ , the evaluation of the drag coefficient at zero lift  $C_{D0}$  is required. A different approach may apply.

Equation (A3) is valid for attached flows. The equation suggested by Barlow et al. [25] uses  $C_{Du}$ —uncorrected drag coefficient—which includes separated flow. Instead, Rogers [24] considered blockage independent of lift and ignored the vortex drag, as long as the flow is attached. Thus, he suggested  $C_{D0} \approx C_{Du}$ .

#### Appendix A.1.3. Drag Coefficient at Zero Lift

The drag coefficient at zero lift is evaluated by the difference between drag coefficient  $C_D$ , defined by reducing the drag force in the usual aerodynamic drag coefficient and the induced drag  $C_{Di} = f(C_L^2)$ . To make this evaluation, it is necessary to make an assumption on the Oswald factor  $e$ . The following formula is applied to small angles of attack:

$$C_{D0} = C_D - \frac{C_L^2}{\pi Re'}, \quad \alpha \leq 5^\circ \tag{A5}$$

A different approach may apply. For instance, Ref. [25] suggests using a linear regression on the uncorrected  $C_{Lu}$  and  $C_{Du}$  data from a preliminary test to get  $C_{D0}$  and  $e$ .

#### Appendix A.1.4. Velocity and Dynamic Pressure Correction

Considering the effects of solid and wake blockages, the flow speed becomes:

$$V_c = V(1 + \epsilon) \tag{A6}$$

where

$$\epsilon = \epsilon_{sb} + \epsilon_{wb} \tag{A7}$$

The dynamic pressure then becomes:

$$q_c = q(1 + \epsilon)^2 \tag{A8}$$

#### Appendix A.1.5. Angle of Attack Correction

It is the sum of the upwash correction and streamline curvature correction as a function of the lift coefficient:

$$\Delta\alpha = \Delta\alpha_{up} + \Delta\alpha_{sc} = \delta \frac{S}{C} C_L + \tau_{2w} \delta \frac{S}{C} C_L = \delta \frac{S}{C} C_L (1 + \tau_{2w}) \tag{A9}$$

where  $\delta$  is the boundary correction factor; it may be found from the charts reported in (Ref. [25], §10.7). The factor  $\tau_{2W}$  is used to manage the amount of correction and here is referred to the wing. Generally,  $\tau_2$  represents the streamline curvature effect on the angle of attack and it may be found from the charts in (Ref. [25], §10.8) using  $\bar{c}/4$  as the tail length variable.

In the original formulation proposed by Barlow et al. [25], there is only the wing lift coefficient  $C_{LW}$  and not the total one  $C_L$ . However, since, in most situations, the horizontal tail provides a little amount of lift compared to the wing, it is useful to use  $C_L$ , which is calculated in real time during a wind tunnel run.

The corrected angle of attack at which the model operates is, therefore, given by the sum of the geometric angle of attack and the correction due to the alteration of the streamlines path by the walls of the closed test section:

$$\alpha_c = \alpha + \Delta\alpha \tag{A10}$$

#### Appendix A.1.6. Lift Coefficient Correction

The lift coefficient is corrected by multiplying the variation due to the effect of streamline curvature by the wing lift curve slope (which should be estimated beforehand):

$$\Delta C_L = \Delta\alpha_{sc} C_{L_{\alpha,W}} = \tau_{2W} \delta \frac{S}{C} C_{L_{\alpha,W}} \tag{A11}$$

This effect is subtracted from the value measured by the wind tunnel balance. In other words, in a closed test section, due to the combined effects of altered streamlines and reduced downwash, the lift produced is greater than that actually expected on the model at the same corrected angle of attack. The corrected lift coefficient then becomes:

$$C_{L_c} = C_L \frac{q}{q_c} - \Delta C_L \tag{A12}$$

In the above equation, the uncorrected  $C_L$  is first modified by the blockage effect, then the correction of the walls is algebraically added.

#### Appendix A.1.7. Drag Coefficient Correction

The drag coefficient is corrected for the effects of the angle of attack change, wake blockage, and buoyancy. Because of the walls, the model in the test section has a too low aerodynamic drag. Therefore, the first term of the following equation has a positive sign, because it must be added to the measurement of the wind tunnel balance. Conversely, the second and third terms have a negative sign because the effects of the model wake in a closed test section and of horizontal buoyancy increase the aerodynamic drag with respect to free air conditions; hence, they must be subtracted from the measurement of the wind tunnel balance:

$$\Delta C_D = \Delta\alpha C_L - \Delta C_{D_{wb}} - C_{D_B} \tag{A13}$$

where the effect of wake blockage is estimated as:

$$\Delta C_{D_{wb}} = \epsilon_{sb} C_{D_0} \tag{A14}$$

while the *buoyancy*  $C_{D_B}$  is a constant of the wind tunnel. Here, the approach of Ref. [24] has been followed, where  $\Delta C_{D_{wb}}$  due to the wake is estimated with the solid blockage  $\epsilon_{sb}$ . Reference [25], §10.9 gives a different and apparently incorrect indication:

$$\Delta C_D = \Delta\alpha_{up} C_{LW} + \delta \frac{S}{C} \frac{1}{C_{LW}^2}$$

where the second term seems to be the effect of the wake blockage, which is added to the upwash effect, but it is inversely proportional to the square of the lift coefficient. Furthermore, the buoyancy effect of the test section is neglected.

Thus, the corrected drag coefficient is the sum of two terms. The first one is evaluated from the measurements of the wind tunnel balance and corrected for blockage effects. The second one is referred to the above cited corrections:

$$C_{Dc} = C_D \frac{q}{q_c} + \Delta C_D \tag{A15}$$

#### Appendix A.1.8. Pitching Moment Coefficient Correction

This correction affects the pitching moment curve slope of the horizontal tailplane only. The curve slope is corrected by accounting for the wall effect, and the streamline curvature effect. Reference [25], §10.9 neglects the streamline curvature effect, after defining and evaluating it in the section about the correction of the angle of attack. It proposes the correction of the pitching moment coefficient as:

$$\Delta C_M = C_{M_{\alpha,H}} \tau_{2H} \delta \frac{S}{C} C_{LW}$$

where the lift coefficient is that of the wing alone.

This effect was discussed earlier as tail downwash change. It occurs in the presence of the horizontal tailplane. In this case, due to the effect of the walls, the wind tunnel model is more stable than in free air conditions. Therefore, the correction in the following equation must be subtracted from the value of the pitching moment coefficient measured by the tunnel balance:

$$\Delta C_M = C_{M_{\alpha,H}} \tau_{2H} \delta \frac{S}{C} C_L + 0.25 \Delta C_L \tag{A16}$$

where  $\tau_{2H}$  is used to manage the amount of correction and is referred to as the tailplane. It is derived as already discussed for Equation (A9). The quantity  $C_{M_{\alpha,H}}$  is the pitching moment curve slope of the horizontal tailplane, which should be estimated from preliminary wind tunnel tests, or calculated as:

$$C_{M_{\alpha,H}} = -C_{L_{\alpha,H}} \eta_H \bar{V}_H \tag{A17}$$

where the negative sign indicates that the horizontal tailplane is situated behind the moment reference point; therefore, contributing to a nose-down pitch for positive lift. The quantity  $\eta_H$  is the dynamic pressure ratio of the tail and the wing. The volumetric ratio is  $\bar{V}_H$ , defined in the usual way:

$$\bar{V}_H = \frac{l_H S_H}{S \bar{c}} \tag{A18}$$

Finally, the corrected moment coefficient is defined as:

$$C_{Mc} = C_M \frac{q}{q_c} - \Delta C_M \tag{A19}$$

### Appendix A.2. Additional Corrections

#### Appendix A.2.1. Evaluation of Zero-Lift Drag Coefficient

The value  $\epsilon_{wb}$  is estimated using Equations (A3) and (A4), where the  $C_{D_0}$  must be known. If this is unknown, it may be computed with Equation (A5) when  $\alpha \approx 0^\circ$ . This requires the attention of the operator to carry out the first measurement at that value of the angle of attack. For all subsequent tests, this calculated  $C_{D_0}$  value should be inserted in the constants file.

The Oswald factor  $e$  can be evaluated with good accuracy using the formula reported in Raymer [30]:

$$e = 1.78(1 - 0.045 \mathcal{R}^{0.68}) - 0.64 \tag{A20}$$

valid for  $3 \leq \mathcal{R} \leq 10$ . However, the ideal would always be to carry out a preliminary wing only (or wing–fuselage) run and then perform a linear regression on the uncorrected experimental data of lift and drag to find  $C_{D_0}$  and  $e$ .

#### Appendix A.2.2. Evaluation of Wing Lift Curve Slope

The wing lift curve slope  $C_{L_{\alpha,W}}$  may be found using a well-known formula [38] for swept wing, with the simplification of Mach number equal to zero:

$$C_{L_{\alpha,W}} = \frac{2\pi\mathcal{R}}{2 + \sqrt{\frac{\mathcal{R}^2}{(C_{\ell_\alpha}/2\pi)^2} \left(1 + \tan^2 \Lambda_{c/2}^2\right) + 4}} \quad (\text{rad}^{-1}) \quad (\text{A21})$$

where the necessary data are all already present in the constants file. The mean profile lift curve slope  $C_{\ell_\alpha}$  can be approximated to  $0.105 \text{ deg}^{-1}$ . Consequently, the constant  $(C_{\ell_\alpha}/2\pi)^2$  can be approximated to 0.9169.

## References

1. National Academies of Sciences Engineering and Medicine. *Commercial Aircraft Propulsion and Energy Systems Research*; The National Academies Press: Washington, DC, USA, 2016. [CrossRef]
2. Moore, M.D.; Fredericks, B. Misconceptions of electric propulsion aircraft and their emergent aviation markets. In Proceedings of the 52nd AIAA Aerospace Sciences Meeting—AIAA Science and Technology Forum and Exposition, SciTech 2014, National Harbor, MD, USA, 13–17 January 2014; pp. 1–17.
3. Dannier, A.; Del Pizzo, A.; Di Noia, L.P.; Spina, I. Sizing Procedure of PMSMs for Hybrid Parallel Aircraft Propulsion. In Proceedings of the 2018 IEEE International Conference on Electrical Systems for Aircraft, Railway, Ship Propulsion and Road Vehicles & International Transportation Electrification Conference (ESARS-ITEC), Nottingham, UK, 7–9 November 2018; pp. 1–6. [CrossRef]
4. Bocii, L.S.; Di Noia, L.P.; Rizzo, R. Optimization of the Energy Storage of Series-Hybrid Propelled Aircraft by Means of Integer Differential Evolution. *Aerospace* **2019**, *6*, 59.
5. ICAO. *Guidance on the Development of States' Action Plan on CO<sub>2</sub> Emissions Reduction Activities (Doc 9988)*; Technical Report; ICAO: Montreal, QC, Canada, 2019.
6. Nicolosi, F.; Marciello, V.; Cusati, V.; Orefice, F. Technology Roadmap and Conceptual Design of Hybrid and Electric Configurations in the Commuter Class. In Proceedings of the 33rd Congress of the International Council of the Aeronautical Sciences, Stockholm, Sweden, 4–9 September 2022.
7. Orefice, F.; Della Vecchia, P.; Ciliberti, D.; Nicolosi, F. Preliminary Design to Fulfil Future Market Demand of Electric Aircraft. *Int. Rev. Aerosp. Eng. (IREASE)* **2021**, *14*, 294. [CrossRef]
8. European Commission. *Flightpath 2050*; Technical Report; European Commission: Brussels, Belgium, 2011; ISBN 9789279197246. [CrossRef]
9. ACARE: Advisory Council for Aeronautics Research in Europe. *2008 Addendum to the Strategic Research Agenda*; Technical Report; Advisory Council for Aeronautics Research in Europe: Brussels, Belgium, 2008.
10. Ciliberti, D.; Della Vecchia, P.; Memmolo, V.; Nicolosi, F.; Wortmann, G.; Ricci, F. The Enabling Technologies for a Quasi-Zero Emissions Commuter Aircraft. *Aerospace* **2022**, *9*, 319. [CrossRef]
11. Perkins, C.D.; Hage, R.E. *Airplane Performance Stability and Control*; Wiley: New York, NY, USA, 1949.
12. Finck, R. *USAF Stability and Control DATCOM*; Report; Wright-Patterson Air Force Base: Greene, OH, USA, 1978.
13. Gilbey, R.W. Contribution of Fin to Sideforce, Yawing Moment and Rolling Moment Derivatives Due to Sideslip,  $(Y_v)_F$ ,  $(N_v)_F$ ,  $(L_v)_F$ , in the Presence of Body, Wing and Tailplane. *Eng. Sci. Data Unit* **1982**, 82010.
14. Pass, R.H. *Analysis of Wind-Tunnel Data on Directional Stability and Control*; Report 775; National Advisory Committee for Aeronautics: Washington, DC, USA, 1940.
15. Sears, R.I. *Wind-Tunnel Data on the Aerodynamic Characteristics of Airplane Control Surfaces*; Wartime Report L-663; National Advisory Committee for Aeronautics: Washington, DC, USA, 1943.
16. Kayten, G.G.; Koven, W. *Comparison of Wind-Tunnel and Flight Measurements of Stability and Control Characteristics of a Douglas A-26 Airplane*; Report 816; National Advisory Committee for Aeronautics: Washington, DC, USA, 1945.
17. Bamber, R.J.; House, R.O. *Wind-Tunnel Investigation of Effect of Yaw on Lateral-Stability Characteristics. II—Rectangular NACA 23012 Wing with a Circular Fuselage and a Fin*; Report 730; National Advisory Committee for Aeronautics: Washington, DC, USA, 1939.
18. House, R.O.; Wallace, A.R. *Wind-Tunnel Investigation of Effect of Interference on Lateral-Stability Characteristics of Four NACA 23012 Wings, an Elliptical and Circular Fuselage and Vertical Fins*; Report 705; National Advisory Committee for Aeronautics: Washington, DC, USA, 1940.
19. Murray, H.E. *Wind-Tunnel Investigation of End-Plate Effects of Horizontal Tails on a Vertical Tail Compared with Available Theory*; Report 1050; National Advisory Committee for Aeronautics: Washington, DC, USA, 1946.



20. Brewer, J.D.; Lichtenstein, J.H. *Effect of Horizontal Tail on Low-Speed Static Lateral Stability Characteristics of a Model Having 45° Sweptback Wing and Tail Surfaces*; Report 2010; National Advisory Committee for Aeronautics: Washington, DC, USA, 1950.
21. Queijo, M.J.; Wolhart, W.D. *Experimental Investigation of the Effect of the Vertical-Tail Size and Length and of Fuselage SHAPE and Length on the Static Lateral Stability Characteristics of a Model with 45° Sweptback Wing and Tail Surfaces*; 1049 Report; National Advisory Committee for Aeronautics: Washington, DC, USA, 1950.
22. Goodman, A. *Effects of Wing Position and Horizontal-Tail Position on the Static Stability Characteristics of Models with Unswept and 45 Degree Sweptback Surfaces with Some Reference to Mutual Interference*; Technical Note TN 2504; National Advisory Committee for Aeronautics: Washington, DC, USA, 1951.
23. Recant, I.C.; Swanson, R.S. *Determination of the Stability and Control Characteristics of Aiplanes from Tests of Powered Models*; Wartime Report L-710; National Advisory Committee for Aeronautics: Washington, DC, USA, 1942.
24. Garner, H.C.; Rogers, E.W.; Acum, W.E.; Maskell, E.C. *Subsonic Wind Tunnel Wall Corrections*; NATO-AGARD: Neuilly sur Seine, France, 1966.
25. Barlow, J.B.; Rae, W.H.; Pope, A. *Low-Speed Wind Tunnel Testing*; Wiley: New York, NY, USA, 1999.
26. Ciliberti, D.; Della Vecchia, P.; Nicolosi, F.; De Marco, A. Aircraft directional stability and vertical tail design: A review of semi-empirical methods. *Prog. Aerosp. Sci.* **2017**, *95*, 140–172. [[CrossRef](#)]
27. Damljanovic, D.; Vukovic, D.; Ocokoljic, G.; Ilic, B.; Rasuo, B. Wind Tunnel Testing of ONERA-M, AGARD-B and HB-2 Standard Models at Off-Design Conditions. *Aerospace* **2021**, *8*, 275. [[CrossRef](#)]
28. Silverstein, A.; Katzoff, S. *Design Charts for Predicting Downwash Angles and Wake Characteristics behind Plain and Flapped Wings*; Technical Report 648; National Advisory Committee for Aeronautics: Washington, DC, USA, 1939.
29. Spreemann, K.P. *Design Guide for Pitch-Up Evaluation and Investigation at High Subsonic Speeds of Possible Limitations Due to Wing-Aspect-Ratio Variations*; Technical Memorandum X-26; NASA Langley Research Center: Washington, DC, USA, 1959.
30. Raymer, D.P. *Aircraft Design: A Conceptual Approach*; American Institute of Aeronautics and Astronautics: Reston, VA, USA, 2012.
31. Finn, R.S. *Effects of External Fuel Tanks and Bombs on Critical Speeds of Aircraft*; Wartime Report L-726; National Advisory Committee for Aeronautics: Washington, DC, USA, 1946.
32. Morris, O.A. *Aerodynamic Forces and Moments on a Large Ogive-Cylinder Store at Various Locations below the Fuselage Center Line of a Swept-Wing Bomber Configuration at a Mach Number of 1.61*; Research Memorandum L56I25; National Advisory Committee for Aeronautics: Washington, DC, USA, 1957.
33. Spearman, M.L. *Some Effects of External Stores on the Static Stability of Fighter Airplanes*; Technical Note D-6775; NASA Langley Research Center: Washington, DC, USA, 1972.
34. Heart Aerospace. Learn More about the ES-30. Available online: <https://heartaerospace.com/es-30/> (accessed on 13 October 2023).
35. Ampaire Inc. Meet the Eco Caravan. Available online: <https://www.ampaire.com/vehicles/eco-caravan> (accessed on 13 October 2023).
36. Shelton, D.B. Removable Cargo Pod with Lifting Mechanism and Open Top. U.S. Patent US8128026B2, 15 January 2009. Available online: <https://patents.google.com/patent/US20090014583A1/en> (accessed on 16 October 2023).
37. Moonan, W.C. Evaluation of the Aerodynamics of an Aircraft Fuselage Pod Using Analytical, CFD, and Flight Testing Techniques. Master's Thesis, University of Tennessee, Knoxville, TN, USA, 2010.
38. Roskam, J. *Methods for Estimating Stability and Control Derivatives of Conventional Subsonic Airplanes*; Roskam Aviation and Engineering Corporation: Lawrence, KS, USA, 1983.

**Disclaimer/Publisher's Note:** The statements, opinions and data contained in all publications are solely those of the individual author(s) and contributor(s) and not of MDPI and/or the editor(s). MDPI and/or the editor(s) disclaim responsibility for any injury to people or property resulting from any ideas, methods, instructions or products referred to in the content.